mater.scichina.com link.springer.com

Published online 6 January 2021 | https://doi.org/10.1007/s40843-020-1562-1
Sci China Mater 2021, 64(7): 1632–1641

Cracked bark-inspired ternary metallic sulfide ($NiCoMnS_4$) nanostructure on carbon cloth for high-performance aqueous asymmetric supercapacitors

Xiao Wang[†], Ling Tian[†], Xiao Long, Mingzhe Yang, Xiaoqiang Song, Wenlu Xie, Dequan Liu, Yujun Fu, Junshuai Li[*], Yali Li[*] and Deyan He

ABSTRACT In this paper, we report a high-performance self-supported supercapacitor electrode composed of a cracked bark-shaped Ni-Co-Mn ternary metallic sulfide ($NiCoMnS_4$) nanostructure on carbon cloth prepared by a simple one-step hydrothermal process and subsequent electrochemical treatment. The electrode delivers a high specific discharge capacity of up to 2470.4 F g^{-1} at 1 A g^{-1} and high rate performances of 1635.6 F g^{-1} at 10 A g^{-1} and 910.2 F g^{-1} even at 32 A g^{-1}. Cycling tests indicate that $NiCoMnS_4$ could maintain >91.1% of its initial capacity and nearly 100% Coulombic efficiency over 10,000 cycles at 8 A g^{-1}. An aqueous asymmetric supercapacitor assembled with $NiCoMnS_4$ as the cathode, activated carbon as the anode, and 1 mol L^{-1} KOH as the electrolyte delivers an energy density of 68.2 W h kg^{-1} at 850.1 W kg^{-1} and capacity retention of 92.5% after 10,000 cycles at 4 A g^{-1}. Given the excellent performance and simple material preparation of our proposed device, this study provides a valuable foundation for the development of self-supported metallic sulfide-based electrodes with high electrochemical properties for potential application in aqueous asymmetric supercapacitors.

Keywords: high-performance self-supported electrodes, ternary metallic sulfide, high specific capacity, aqueous asymmetric supercapacitors, high energy density

INTRODUCTION

Electrochemical energy storage is one of the most commonly used energy-storage technologies available today. Lithium-ion (Li^+) batteries occupy a large proportion of the energy-storage market and are extensively used in electric vehicles and mobile electronic devices, such as cell phones, laptops, and digital cameras, on account of their high energy density, operating voltage, and safety and long lifetime [1–8]. However, the relatively low power density and limited and uneven distribution of Li resources are the main bottlenecks associated with Li^+ batteries [9,10]. Compared with Li^+ batteries, supercapacitors have much higher power densities; these capacitors can collect energy within a very short time (e.g., <1 min) and release it when needed. Moreover, numerous material choices are available for supercapacitors. Thus, research on supercapacitors has attracted intense attention and seen great progress [11–15].

Among the various types of supercapacitors available commercially, those based on aqueous electrolytes are of particular interest because of their high safety, low cost, and good environmental friendliness [16–20]. However, given the low electrochemical stability of water, improvements in energy density, which are vital for the practical applications of aqueous supercapacitors, are difficult to implement by simply increasing the working voltage. Developing novel electrode materials/structures with high capacity has been proposed to be an important direction in enhancing the energy density of aqueous supercapacitors [21–26]. Transition metal (e.g., Mn, Co, Ni) oxides usually have relatively high theoretical capacities; unfortunately, these capacities are challenging to realize in practice because the metal oxides have poor electrical conductivity, which partly originates from their wide bandgap, and limited availability of active sites, especially in the bulk phase [27–30]. Compared with their oxide counterparts, transition metal sulfides have a narrower bandgap; the electrochemical and electrical prop-

Key Laboratory of Special Function Materials & Structure Design of the Ministry of Education, and School of Physical Science & Technology, Lanzhou University, Lanzhou 730000, China
[†] These authors contributed equally to this work.
[*] Corresponding authors (emails: jshli@lzu.edu.cn (Li J); liyli@lzu.edu.cn (Li Y))

erties of these materials can easily be adjusted by forming polymetallic sulfides that may potentially be used to realize high-performance supercapacitor electrodes [31–34].

In this study, a high-performance self-supported supercapacitor electrode composed of a cracked bark-shaped Ni–Co–Mn ternary metallic sulfide ($NiCoMnS_4$) on carbon cloth (CC) was developed *via* a simple one-step hydrothermal process and subsequent electrochemical treatment. The electrode can deliver a high specific discharge capacity of up to 2470.4 F g^{-1} at 1 A g^{-1} and good rate performances of 1635.6 F g^{-1} at 10 A g^{-1} and 910.2 F g^{-1} even at 32 A g^{-1}. $NiCoMnS_4$ can retain 91.1% of its initial capacity after 10,000 cycles at 8 A g^{-1}, thus demonstrating its high cycling performance. An aqueous asymmetric supercapacitor (ASC) composed of $NiCoMnS_4$ as the cathode, activated carbon (AC) as the anode, and 1 mol L^{-1} KOH as the electrolyte could deliver an energy density of up to 68.2 W h kg^{-1} at 850.1 W kg^{-1} and retain 92.5% of its capacity after 10,000 cycles at 4 A g^{-1}.

EXPERIMENTAL SECTION

Materials

All of the chemicals in the experiment were of analytical grade and used as received without further purification. CC (thickness, 0.33 mm), nickel foam (NF; thickness, 1.0 mm), AC, acetylene black, polyvinylidene fluoride (PVDF), and *N*-methyl pyrrolidone (NMP) were obtained from commercial suppliers.

Preparation of electrode materials and assembly of ASC

Hydrophilic treatment of CC: CC was first cut into pieces measuring 1.0 cm × 2.0 cm and then ultrasonically cleaned in acetone, ethanol, and deionized (DI) water in sequence for 15 min each time. Hydrophilic treatment of the dried CC (60°C in an air oven) was conducted by immersing it in a mixed solution of 98 wt% H_2SO_4 and 68 wt% HNO_3 at a volume ratio of 1:3 and then transferring it into an 80-mL Teflon-lined stainless steel autoclave. The autoclave was sealed and heated at 90°C for 6 h. After being cooled to room temperature, the CC pieces were rinsed several times with DI water to wash off the acids and ultrasonically treated for 1 h to eliminate weakly adhered carbon materials. Thereafter, the CC pieces were dried in vacuum.

Preparation of cracked bark-shaped $NiCoMnS_4$ on CC: In a typical synthetic procedure, as illustrated in Fig. 1, 75 mg of $Co(NO_3)_2{\cdot}6H_2O$, 75 mg of $MnSO_4{\cdot}H_2O$, and 150 mg of H_2NCSNH_2 were dissolved in 40 mL of DI water with magnetic stirring for 15 min to obtain a transparent light-pink solution. Next, a piece of NF (1.0 cm × 1.0 cm) and two pieces of CC were immersed in

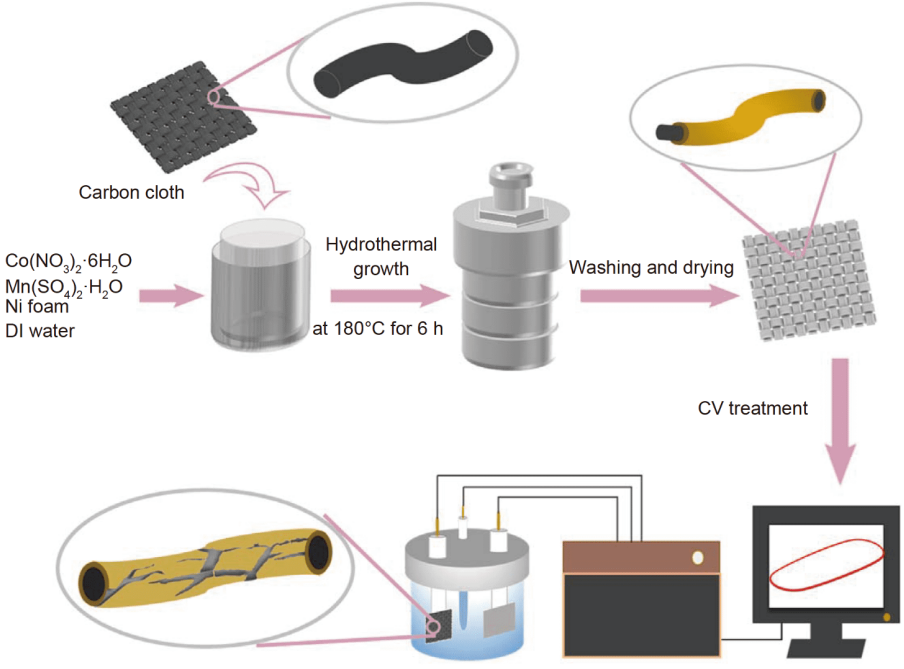

Figure 1 Schematic of the synthetic procedure for the cracked bark-shaped $NiCoMnS_4$ on CC.

the above solution, transferred into a Teflon-lined stainless steel autoclave, and maintained at 180°C for 6 h. After being cooled to room temperature naturally, the CC pieces were obtained, washed several times with DI water to remove any unreacted residues, and dried overnight at 60°C in an air oven. The samples were electrochemically treated by cyclic voltammetry (CV) at a rate of 50 mV s^{-1} in the potential window of 0–0.45 V for 200 cycles to form a cracked bark-shaped nanostructure. The mass loading of the active material on CC was approximately 0.5 mg cm^{-2}.

Assembly of ASC: First, AC anodes were prepared by mixing AC, acetylene black, and PVDF at a mass ratio of 8:1:1 with NMP. The mixture was hand-ground for at least 30 min to obtain a slurry, which was then coated onto CC with hydrophilic treatment and dried overnight at 60°C in an air oven. Next, the ASC was assembled using $NiCoMnS_4$ on CC as the cathode, AC on CC as the anode, 1 mol L^{-1} KOH solution as the electrolyte, and porous polypropylene membrane as the separator. The lighting device used to test the applicability of the ASC was composed of a red light-emitting diode (LED) with 2016 coin cells.

A supercapacitor can be stably operated in a wide voltage window if the active mass ratio of the cathode to the anode is carefully decided according to the charge balance equation $m_+/m_- = (C_-\Delta V_-)/(C_+\Delta V_+)$ [35], where m_+ and m_- are the active masses, C_+ and C_- are the specific capacitances obtained by three-electrode testing, and ΔV_+ and ΔV_- are the voltage windows of the cathode and anode, respectively. Because the respective specific capacitances of $NiCoMnS_4$ and AC were calculated to be 1170.8 and 190.8 F g^{-1} in the potential windows of 0–0.45 V and −1.1–0 V (at 15 mV s^{-1}), the optimized mass loading of AC was estimated to be 2.5 mg cm^{-2}.

Physical characterization

X-ray diffractometry (XRD, X'Pert Philips) and micro-Raman spectroscopy (Jobin-Yvon Horiba HR800; excitation wavelength, 532 nm) were employed to analyze the material phase. Scanning electron microscopy (SEM, MIRA3, TESCAN) and transmission electron microscopy (TEM, FEI Tecnai G^2 F30) were used to characterize the morphology and microstructures of the samples, respectively. Elemental and surface chemical compositions were analyzed by X-ray photoelectron spectroscopy (XPS, Escalab 250xi). The Brunauer–Emmett–Teller (BET, ASAP 2020 Micromeritics) specific surface area of the material was obtained *via* its N_2 adsorption/desorption isotherms at 77 K, and the pore size distribution was calculated from the adsorption curve using the Barrett–Joyner–Halenda (BJH) method. The contents of Ni, Co, Mn, and S in the material were determined by inductively coupled plasma–atomic emission spectrometry (ICP-AES), and elemental mappings were recorded by an energy-dispersive X-ray spectrometer(EDS, Octane Ultra).

Electrochemical measurements

The electrochemical properties of the electrodes were measured using an electrochemical workstation (CHI660E, CH Instruments, Shanghai) with a three-electrode electrochemical cell containing 1 mol L^{-1} KOH aqueous solution as the electrolyte and $NiCoMnS_4$ on CC and AC on CC as the working electrodes.

Pt foil measuring 2.0 cm × 2.0 cm was used as the counter electrode, and a Ag/AgCl electrode served as the reference electrode. CV, galvanostatic charge/discharge (GCD) tests, and electrochemical impedance spectroscopy (EIS) were conducted at room temperature. The mass specific capacity, C_s (F g^{-1}), was calculated according to the discharge time using the equation $C_s = (I \times \Delta t)/(m \times \Delta V)$, where I (A) is the constant discharge current, Δt (s) is the discharge time, m (g) is the active mass of the working electrode, and ΔV (V) is the discharge voltage [36]. The energy density (E) and power density (P) of the ASC devices were respectively calculated using the equations $E = C_s V^2/7.2$ and $P = 3600E/\Delta t$, where C_s (F g^{-1}), V (V), and Δt (s) are the specific capacity based on the total mass of the active materials in the cathode and anode, the working voltage, and the discharge duration of the supercapacitors, respectively.

RESULTS AND DISCUSSION

After hydrothermal growth, $NiCoMnS_4$ is evenly coated on CC, as revealed in Fig. S1. However, after 200 cycles of CV at 50 mV s^{-1} in the potential window of 0–0.45 V, significant changes in the morphology of the $NiCoMnS_4$ film occurred, and a cracked bark-shaped structure formed, as indicated by the SEM images shown Fig. 2a, b. This development could be attributed to enhancements in K^+ intercalation/de-intercalation into the $NiCoMnS_4$ film at high current densities, which lead to internal stress accumulation in the film and subsequent cracking [37,38]. Electrochemical treatment at CV scan rates of 5, 10, 20, 30, 60, and 100 mV s^{-1} in the potential window of 0–0.45 V was performed for 200 cycles to test this supposition. As demonstrated by the SEM images shown in Fig. S2, the $NiCoMnS_4$ film morphology shows only slight changes at low scan rates because of the negligible impact of K^+ intercalation/de-intercalation. When the scan rate

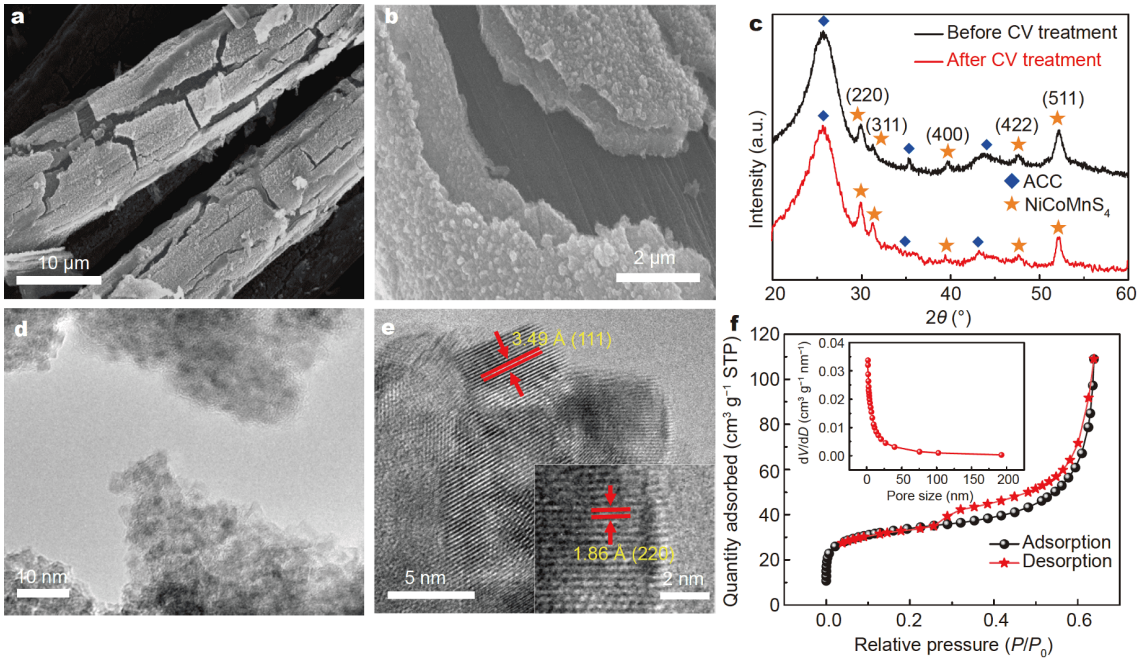

Figure 2 (a) Low- and (b) high-magnification SEM images of the cracked bark-shaped $NiCoMnS_4$ nanostructure on CC. (c) XRD patterns of $NiCoMnS_4$ on CC before and after CV treatment. (d) Low- and (e) high-magnification TEM micrographs of the cracked bark-shaped $NiCoMnS_4$. (f) N_2 adsorption/desorption isotherms (inset: BJH plot of the pore size distribution) of the cracked bark-shaped $NiCoMnS_4$.

reaches 30 mV s^{-1}, cracks emerge. At higher scan rates, i.e., 60 and 100 mV s^{-1}, severe cracking leading to the peeling of the $NiCoMnS_4$ film from the CC is observed. Thus, we selected the scan rate of 50 mV s^{-1} for electrochemical treatment to form the desired cracked bark-shaped structure. However, considering the complexity of the formation of the cracked bark-shaped structure, more investigations regarding this subject may be necessary.

The XRD patterns shown in Fig. 2c confirm that the as-synthesized material is cubic-type $NiCoMnS_4$ (JCPDS Card No. 20-0782). Electrochemical treatment does not evidently change the material phase, as verified by the Raman spectra shown in Fig. S3 [39,40]. ICP-AES measurements confirm that Ni, Co, Mn, and S exist at a stoichiometric ratio consistent with that expected for $NiCoMnS_4$. These four elements are uniformly distributed in the sample, as indicated by the elemental mappings shown in Fig. S4. The cracked bark-shaped structure of $NiCoMnS_4$ endows it with improved electrochemical performance and stability by providing increased specific surface area/active sites and a noncompact structure [41].

A TEM micrograph of $NiCoMnS_4$ is shown in Fig. 2d, e. The material is composed of tiny crystals with relatively uniform sizes. The high-resolution TEM image in Fig. 2e shows lattice fringes with interplanar distances of 1.86 and 3.49 Å, which respectively correspond to the (220) and (111) crystal planes of cubic $NiCoMnS_4$. These findings are consistent with our XRD patterns and a previous report [40]. BET measurement of the cracked bark-shaped $NiCoMnS_4$ was conducted to understand its microstructure further, and the corresponding N_2 adsorption/desorption isotherms, together with the pore size distribution, are shown in Fig. 2f. The type-IV sorption behavior observed reveals the mesoporous structure of the cracked bark-shaped $NiCoMnS_4$. This finding is confirmed by the BJH plot of the pore size distribution shown in the inset, which shows a BET specific area as high as 102.6 m^2 g^{-1} [42].

The chemical compositions and oxidation states of the metal cations in $NiCoMnS_4$ were characterized by XPS, and the spectra obtained are shown in Fig. 3. The survey spectrum in Fig. 3a confirms the presence of Ni, Co, Mn, and S from $NiCoMnS_4$ and C from CC. O and N are attributed to adsorbed O-containing contaminants, such as O_2, CO_2, and H_2O, oxidation of $NiCoMnS_4$/CC during the experiment and storage, and the hydrophilic treatment of CC using a solution containing HNO_3 [43]. Fig. 3b shows the high-resolution Ni 2p spectrum. The two spin-orbit doublet states observed at approximately

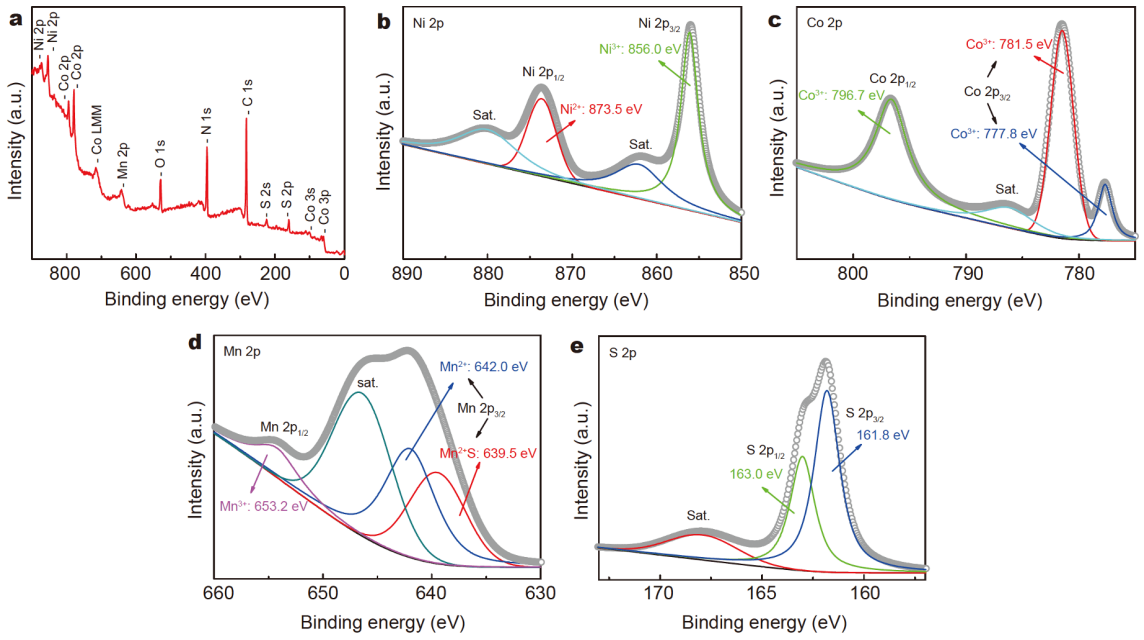

Figure 3 (a) Full XPS survey spectrum of $NiCoMnS_4$ on CC. High-resolution spectra of (b) Ni 2p, (c) Co 2p, (d) Mn 2p, and (e) S 2p.

856.0 eV (Ni $2p_{3/2}$) and 873.5 eV (Ni $2p_{1/2}$) are associated with Ni^{3+} and Ni^{2+}, respectively [49]. The high-resolution spectrum of Co 2p in Fig. 3c reveals two peaks located at approximately 777.8 and 781.5 eV (Co $2p_{3/2}$) , which could be attributed to the existence of Co^{3+}, and another peak at 796.7 eV (Co $2p_{1/2}$), which could be associated with Co^{2+}. Fig. 3d reveals the high-resolution spectrum of Mn 2p . The two peaks located at approximately 642.0 and 639.5 eV correspond to the spin-orbit doublet states of Mn $2p_{3/2}$ and the peak located at approximately 653.2 eV reflects Mn $2p_{1/2}$, thus indicating the presence of Mn^{2+} and Mn^{3+}, respectively [44]. The spectrum of S is shown in Fig. 3e. Two main peaks are observed at 163.0 eV (S $2p_{1/2}$) and 161.8 eV (S $2p_{3/2}$). The peak at 161.8 eV is attributed to S^{2-} with a low coordination number on the surface of the material, and the peak at 163.0 eV originates from S-metal bonds. Another S 2p peak at approximately 168.1 eV is assigned to surface S species of higher oxidation states [31]. The XPS spectra indicate the presence of Ni, Co, and Mn of various valence states, which would confer $NiCoMnS_4$ with excellent charge storage ability.

Comparison of the CV characteristics of the cracked bark-shaped $NiCoMnS_4$ on CC and pure CC of the same size, i.e., 1.0 cm × 2.0 cm, was first conducted for electrochemical characterization. As revealed in Fig. 4a, the capacity contribution from CC is negligible when compared with that from $NiCoMnS_4$. Fig. 4b shows the CV curves of the electrode at various scan rates in the potential window of 0–0.45 V. The electrode shows good reversibility, as evidenced by the excellent retention of its curve shape despite increases in scan rate. Moreover, as the scan rate increases, the anodic and cathodic peaks shift toward more positive and negative potentials, respectively, which is mainly due to the inability of electrolyte ions to diffuse toward the inner electrode surface. This lagged redox response to the potential scan rate results in the polarization of the electrodes at higher scan rates, leading to an incomplete redox reaction and reduced C_s [50].

GCD curves were recorded using 1 mol L^{-1} KOH electrolyte in the potential range of 0–0.45 V at various current densities to evaluate the electrochemical performance of the cracked barked-shaped $NiCoMnS_4$ electrode further. As demonstrated in Fig. 4c, the symmetric charge/discharge curves of the electrode demonstrate its good supercapacitive performance, high Coulombic efficiency, and excellent reversibility [45]. The calculated C_s values are as high as ~2470.4, 2282.7, 2060.4, 1760.0, and 1635.6 F g^{-1} at current densities of 1.0, 2.0, 4.0, 8.0, and 10.0 A g^{-1}, respectively. These data reflect the high rate performance of $NiCoMnS_4$. A C_s of 910.2 F g^{-1} could be achieved even at 32 A g^{-1} (Fig. S5; GCD curves at 16 and 32 A g^{-1}). Fig. 4d shows the Nyquist plot of the EIS curve of the cracked bark-shaped $NiCoMnS_4$ on CC. The steep linear trend observed at low frequencies indicates good

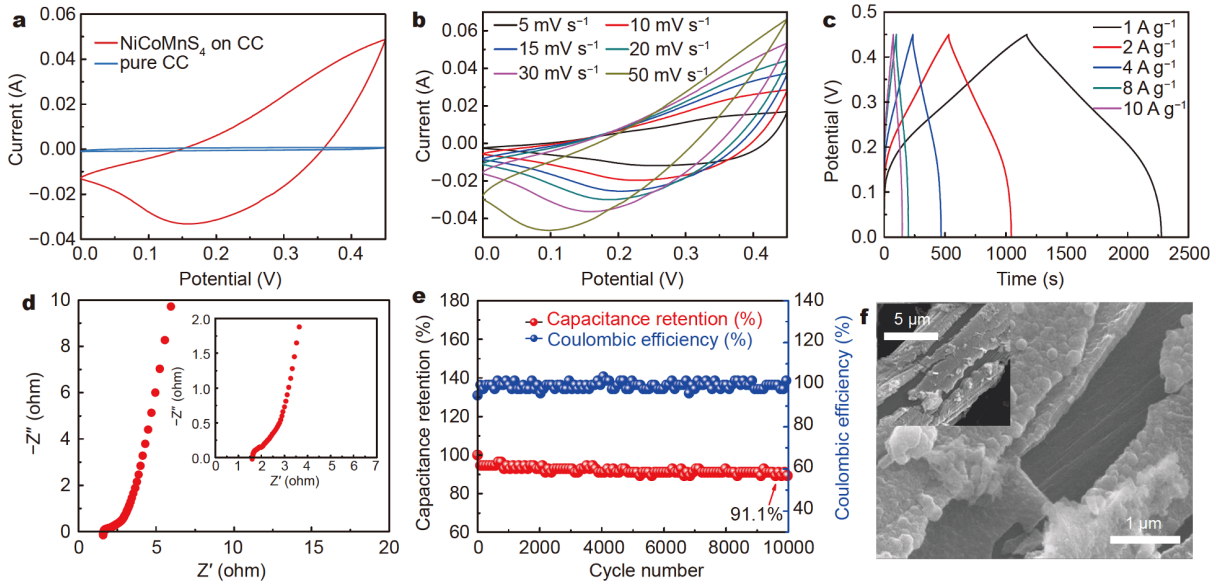

Figure 4 (a) Comparison of the CV curves of cracked bark-shaped $NiCoMnS_4$ on CC and pure CC at 20 mV s^{-1}. (b) CV, (c) GCD curves of the cracked bark-shaped $NiCoMnS_4$ on CC at various scan rates in the potential window of 0.0–0.45 V. (d) Nyquist plot of the cracked bark-shaped $NiCoMnS_4$ on CC. Inset: Enlarged plot at high frequency. (e) Cycling performance and Coulombic efficiency at 8 A g^{-1}. (f) SEM image of cracked bark-shaped $NiCoMnS_4$ on CC after 10,000 cycles at 8 A g^{-1}.

capacitive behavior. The intersection of the EIS curve with the *x* axis occurs at approximately 1.62 Ω (Fig. 4d, inset), which indicates a small series resistance that could be attributed to the fast electron transport network introduced by CC and the improved contact between the cracked bark-shaped electrode material and the electrolyte [47]. The diameter of the semicircle in the EIS curve at moderate frequency, at ~0.41 Ω, indicates a small charge transfer impedance, as seen in the inset of Fig. 4d [48]. The equivalent circuit simulated on the basis of the EIS curve is schematized in Fig. S6.

Fig. 4e shows the cycling performance and Coulombic efficiency of the cracked bark-shaped $NiCoMnS_4$ on CC measured at 8 A g^{-1}. Approximately 91.1% of its initial capacity could be retained by the electrode even after 10,000 cycles, thus revealing its outstanding long-term cycling stability. In addition, the Coulombic efficiency of $NiCoMnS_4$ is approximately 100% after 10,000 cycles, thus demonstrating a highly reversible Faradic reaction between the electrode and electrolyte. The morphology of the electrode was characterized by SEM after the cycling test to understand its cycling performance better. As shown in Fig. 4f, the cracked bark-shaped structure is well maintained even after 10,000 cycles at 8 A g^{-1}. XRD and TEM were conducted to assess changes in the microstructures after the cycling test. The XRD pattern and high-resolution TEM image shown in Fig. S7 reveal the amorphization of the polycrystalline structure of $NiCoMnS_4$ (before cycling; Fig. 2e) after cycling; amorphization helps create more defects/active sites and effectively relieves stress during charging/discharging. The combination of this feature with the well-maintained cracked bark-shaped morphology of the nanostructures is beneficial to the cycling stability of the material. The electrochemical performances of previously reported electrode materials based on similar material systems are summarized and compared with that observed in this study in Table 1. Among the materials listed in the Table, the cracked bark-shaped $NiCoMnS_4$ nanostructure on CC appears to deliver the best comprehensive performance.

Following our evaluation of the electrochemical performance of single electrodes, an aqueous ASC employing the cracked bark-shaped $NiCoMnS_4$ on CC as the self-standing cathode, AC on CC as the anode (see the anode preparation procedure in the experimental section and the electrochemical performance of this electrode in Fig. S8), 1 mol L^{-1} KOH solution as the electrolyte, and porous polypropylene membrane as the separator was assembled and denoted as $NiCoMnS_4$//AC. Fig. 5a shows the CV curves of the cathode and anode of the device recorded at a scan rate of 15 mV s^{-1} in the potential windows of 0–0.45 V and −1.1–0 V, respectively. The capacities of the cathode and anode are matched. The CV curves of $NiCoMnS_4$//AC in different voltage windows at

Table 1 Summary and comparison of the electrochemical properties of the proposed and previously reported electrodes with similar material systems

Sample	Synthesis method	Capacity (F g^{-1})	Cycle stability (cycle number)	Ref.
NiCoMnS	Cathodic electrodeposition	2717	80.0% (1000)	[28]
$MnCo_2S_4$	Hydrothermal	2067	80.2% (6000)	[48]
$CoNi_2S_4$	Potentiostatic deposition	1932	89.2% (1000)	[49]
$MnCo_2S_4$	Hydrothermal	1812	86.1% (5000)	[46]
$CoNi_2S_4$-rGO	Hydrothermal	1680	57.0% (5000)	[50]
Ni-Co-Mn hydroxide	Hydrothermal	1400	114.0% (10,000)	[45]
Ni–Co–Mn hydroxide	one-pot hydrothermal	1188	–	[18]
$NiCoMnS_4$	One-step hydrothermal + electrochemical treatment	2470	91.1% (10,000)	This work

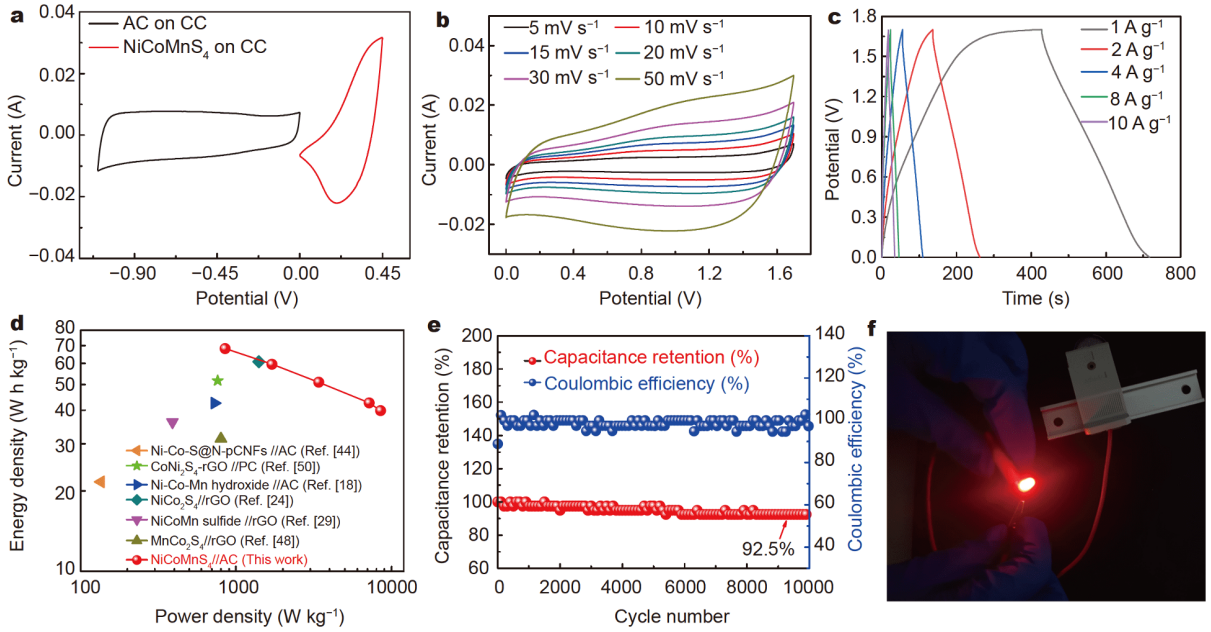

Figure 5 (a) CV curves of the cathode and anode recorded at a scan rate of 15 mV s^{-1} in separate potential windows. (b) CV curves of the ASC at varying scan rates in the voltage window of 0.0–1.7 V. (c) GCD curves of the ASC at different current densities in the voltage window of 0.0–1.7 V. (d) Ragone plot of the ASC and performance comparison with previously reported aqueous supercapacitors employing Ni-Co-Mn-based cathodes. (e) Cycling performance and Coulombic efficiency of the electrode after 10,000 cycles at 4 A g^{-1}. (f) Photograph of a red LED with a nominal voltage of 3.2–3.4 V lit by two serially connected coin cells.

a scan rate of 20 mV s^{-1} are shown in Fig. S9, which illustrates that the voltage window of 0–1.7 V could be delivered by the ASC. Fig. 5b shows the CV curves of the aqueous ASC at various scan rates in the voltage window of 0–1.7 V. The shape of the CV curve is remarkably constant, thus revealing good reversibility. The GCD curves recorded at different current densities in the voltage window of 0–1.7 V are shown in Fig. 5c. Specific capacities of ~170.1, 148.6, 127.1, 106.4, and 99.4 F g^{-1} could be achieved at 1.0, 2.0, 4.0, 8.0, and 10.0 A g^{-1}, respectively.

Because of its high specific capacity and acceptable voltage window, $NiCoMnS_4$//AC may be expected to deliver a relatively high energy density. Fig. 5d shows the Ragone plot of our ASC in comparison with those of previously reported supercapacitors. Energy densities of as high as ~68.2 W h kg^{-1} at a power density of 850.1 W kg^{-1} and ~39.9 W h kg^{-1} even at 8499.4 W kg^{-1} could be achieved by our electrode, thus revealing its superior energy-storage performance compared with

other aqueous supercapacitors based on similar cathode material systems, such as Ni-Co-S//N-pCNFs (21.6 W h kg^{-1} at 135.0 W kg^{-1}) [44], $CoNi_2S_4$-rGO//PC (51.7 W h kg^{-1} at 762.0 W kg^{-1}) [50], Ni-Co-Mn hydroxide//AC (42.6 W h kg^{-1} at 726.1 W kg^{-1}) [18], $NiCo_2S_4$//rGO (60.9 W h kg^{-1} at 1400 W kg^{-1}) [24], NiCoMn sulfide//rGO (36.2 W h kg^{-1} at 390.0 W kg^{-1}) [29], and $MnCo_2S_4$ (31.3 W h kg^{-1} at 800.0 W kg^{-1}) [48]. Cycling tests indicate the excellent stability of $NiCoMnS_4$ with a high capacity retention of up to 92.5% and ~100% Coulombic efficiency after 10,000 cycles at 4 A g^{-1}, as illustrated in Fig. 5e. A red LED with a nominal voltage of 3.2–3.4 V was lit using two coin cells connected in series to evaluate the practicability of our aqueous ASC (Fig. 5f). As shown in Fig. S10, a light duration of up to 11 min is recorded.

CONCLUSIONS

In this study, a high-performance self-supported supercapacitor electrode consisting of a cracked bark-shaped $NiCoMnS_4$ nanostructure on CC was developed by a simple one-step hydrothermal process and subsequent electrochemical treatment. The electrode delivered a specific discharge capacity of as high as 2470.4 F g^{-1} at 1 A g^{-1} and showed good rate performances of 1635.6 F g^{-1} at 10 A g^{-1} and 910.2 F g^{-1} even at 32 A g^{-1}. Cyclic tests indicated that ~91.1% of the initial capacity of the electrode and nearly 100% Coulombic efficiency could be maintained over 10,000 cycles at 8 A g^{-1}. An aqueous ASC assembled with $NiCoMnS_4$ as the cathode, AC as the anode, and 1 mol L^{-1} KOH as the electrolyte provided an energy density of up to 68.2 W h kg^{-1} at 850.1 W kg^{-1} and capacity retention of 92.5% after 10,000 cycles at 4 A g^{-1}. Given the excellent performance and simple material preparation of our proposed device, this study provides a valuable foundation for the development of self-supported metallic sulfide-based electrodes with good electrochemical properties for potential application in aqueous asymmetric supercapacitors.

Received 11 September 2020; accepted 13 November 2020; published online 6 January 2021

1 Miller JR, Simon P. Electrochemical capacitors for energy management. Science, 2008, 321: 651–652
2 Deng L, Li W, Li H, *et al.* A hierarchical copper oxide–germanium hybrid film for high areal capacity lithium ion batteries. Front Chem, 2019, 7: 869
3 Zhu J, Li Y, Yang B, *et al.* A dual carbon-based potassium dual ion battery with robust comprehensive performance. Small, 2018, 14: 1801836
4 Wang J, Wang X, Lee SW, *et al.* Enhanced performance of an electric double layer microsupercapacitor based on novel carbon-encapsulated Cu nanowire network structure as the electrode. ACS Appl Mater Interfaces, 2019, 11: 40481–40489
5 Yang J, Liu J, Zhao C, *et al.* Core-shell structured heterohierachical porous Si@graphene microsphere for high-performance lithium-ion battery anodes. Mater Lett, 2020, 266: 127484
6 Zhu J, Xu Y, Fu Y, *et al.* Hybrid aqueous/nonaqueous water-in-bisalt electrolyte enables safe dual ion batteries. Small, 2020, 16: 1905838
7 Han C, Zhu J, Zhi C, *et al.* The rise of aqueous rechargeable batteries with organic electrode materials. J Mater Chem A, 2020, 8: 15479–15512
8 Simon P, Gogotsi Y. Materials for electrochemical capacitors. Nat Mater, 2008, 7: 845–854
9 Li M, Lu J, Chen Z, *et al.* 30 years of lithium-ion batteries. Adv Mater, 2018, 30: 1800561
10 Jia L, Li Y, Su L, *et al.* TiO_2 nanoparticles *in situ* formed on Ti_3C_2 nanosheets by a one-step ethanol-thermal method for enhanced reversible lithium-ion storage. ChemistrySelect, 2020, 5: 3124–3129
11 Tang Y, Chen T, Yu S, *et al.* A highly electronic conductive cobalt nickel sulphide dendrite/quasi-spherical nanocomposite for a supercapacitor electrode with ultrahigh areal specific capacitance. J Power Sources, 2015, 295: 314–322
12 Ding Y, Yang B, Chen J, *et al.* Nanotube-like hard carbon as high-performance anode material for sodium ion hybrid capacitors. Sci China Mater, 2018, 61: 285–295
13 Wang C, Xu J, Yuen MF, *et al.* Hierarchical composite electrodes of nickel oxide nanoflake 3D graphene for high-performance pseudocapacitors. Adv Funct Mater, 2015, 24: 6372–6380
14 Liu H, Zhang Y, Dong J, *et al.* Curving effects of concave dodecahedral nanocarbons enable enhanced Li-ion storage. J Mater Chem A, 2018, 6: 14894–14902
15 Guo H, Liu L, Dou Q, *et al.* Punching holes on paper-like electrodes: An effective strategy to enhance rate performance of supercapacitors. Energy Storage Mater, 2019, 19: 338–345
16 Wang J, Tian L, Xie W, *et al.* A hierarchical interconnected nanosheet structure of porous δ-MnO_2 on graphite paper as cathode with a broad potential window for $NaNO_3$ aqueous electrolyte supercapacitors. ACS Appl Energy Mater, 2020, 3: 2614–2622
17 Tang Y, Chen S, Mu S, *et al.* Synthesis of capsule-like porous hollow nanonickel cobalt sulfides *via* cation exchange based on the kirkendall effect for high-performance supercapacitors. ACS Appl Mater Interfaces, 2016, 8: 9721–9732
18 Sivakumar P, Jana M, Jung MG, *et al.* Hexagonal plate-like Ni–Co–Mn hydroxide nanostructures to achieve high energy density of hybrid supercapacitors. J Mater Chem A, 2019, 7: 11362–11369
19 Meng A, Shen T, Huang T, *et al.* $NiCoSe_2/Ni_3Se_2$ lamella arrays grown on N-doped graphene nanotubes with ultrahigh-rate capability and long-term cycling for asymmetric supercapacitor. Sci China Mater, 2020, 63: 229–239
20 Han X, Tao K, Wang D, *et al.* Design of a porous cobalt sulfide nanosheet array on Ni foam from zeolitic imidazolate frameworks as an advanced electrode for supercapacitors. Nanoscale, 2018, 10: 2735–2741
21 Yao T, Guo X, Qin S, *et al.* Effect of rGO coating on interconnected Co_3O_4 nanosheets and improved supercapacitive behavior of Co_3O_4/rGO/NF architecture. Nano-Micro Lett, 2017, 9: 38
22 Ding Y, Li Y, Li J, *et al.* High-performance nitrogen and sulfur co-doped nanotube-like carbon anodes for sodium ion hybrid capacitors. Chin Chem Lett, 2020, 31: 2219–2224

23 Chen J, Yang B, Li H, *et al.* Candle soot: onion-like carbon, an advanced anode material for a potassium-ion hybrid capacitor. J Mater Chem A, 2019, 7: 9247–9252
24 Annamalai KP, Liu L, Tao Y. Highly exposed nickel cobalt sulfide–rGO nanoporous structures: an advanced energy-storage electrode material. J Mater Chem A, 2017, 5: 9991–9997
25 Long X, Tian L, Wang J, *et al.* Interconnected δ-MnO_2 nanosheets anchored on activated carbon cloth as flexible electrode for high-performance aqueous asymmetric supercapacitors. J Electroanal Chem, 2020, 877: 114656
26 Guo Y, Yang J, Wu D, *et al.* Au nanoparticle-embedded, nitrogen-deficient hollow mesoporous carbon nitride spheres for nitrogen photofixation. J Mater Chem A, 2020, 8: 16218–16231
27 Yao T, Li Y, Liu D, *et al.* High-performance free-standing capacitor electrodes of multilayered Co_9S_8 plates wrapped by carbonized poly (3,4-ethylenedioxythiophene):poly(styrene sulfonate)/reduced graphene oxide. J Power Sources, 2018, 379: 167–173
28 Sahoo S, Mondal R, Late DJ, *et al.* Electrodeposited nickel cobalt manganese based mixed sulfide nanosheets for high performance supercapacitor application. Microporous Mesoporous Mater, 2017, 244: 101–108
29 Sanchez JS, Pendashteh A, Palma J, *et al.* Insights into charge storage and electroactivation of mixed metal sulfides in alkaline media: NiCoMn ternary metal sulfide nano-needles forming core–shell structures for hybrid energy storage. J Mater Chem A, 2019, 7: 20414–20424
30 Han X, Wang B, Yang C, *et al.* Inductive effect in Mn-doped NiO nanosheet arrays for enhanced capacitive and highly stable hybrid supercapacitor. ACS Appl Energy Mater, 2019, 2: 2072–2079
31 He W, Wang C, Li H, *et al.* Ultrathin and porous Ni_3S_2/$CoNi_2S_4$ 3D-network structure for superhigh energy density asymmetric supercapacitors. Adv Energy Mater, 2017, 7: 1700983
32 Qin S, Yao T, Guo X, *et al.* MoS_2/Ni_3S_4 composite nanosheets on interconnected carbon shells as an excellent supercapacitor electrode architecture for long term cycling at high current densities. Appl Surf Sci, 2018, 440: 741–747
33 Xu X, Liu W, Kim Y, *et al.* Nanostructured transition metal sulfides for lithium ion batteries: Progress and challenges. Nano Today, 2014, 9: 604–630
34 Chen W, Xia C, Alshareef HN. One-step electrodeposited nickel cobalt sulfide nanosheet arrays for high-performance asymmetric supercapacitors. ACS Nano, 2014, 8: 9531–9541
35 Meng G, Yang Q, Wu X, *et al.* Hierarchical mesoporous NiO nanoarrays with ultrahigh capacitance for aqueous hybrid supercapacitor. Nano Energy, 2016, 30: 831–839
36 Yang C, Wang X, Dong W, *et al.* Nitrogen-doped black titania for high performance supercapacitors. Sci China Mater, 2020, 63: 1227–1234
37 Wang D, Wu X, Wang Z, *et al.* Cracking causing cyclic instability of $LiFePO_4$ cathode material. J Power Sources, 2005, 140: 125–128
38 Woodford WH, Chiang YM, Carter WC. "Electrochemical shock" of intercalation electrodes: a fracture mechanics analysis. J Electrochem Soc, 2010, 157: A1052
39 Pendashteh A, Sanchez JS, Palma J, *et al.* Anchored $NiCoMnS_4$ nanoparticles on N-doped rGO: High-performance bifunctional electrocatalysts for rechargeable Zn-air batteries. Energy Storage Mater, 2019, 20: 216–224
40 Xia C, Li P, Gandi AN, *et al.* Is $NiCo_2S_4$ really a semiconductor? Chem Mater, 2015, 27: 6482–6485
41 Li Q, Li L, Owusu KA, *et al.* Self-adaptive mesoporous CoS @alveolus-like carbon yolk-shell microsphere for alkali cations storage. Nano Energy, 2017, 41: 109–116
42 Chen X, Shi T, Zhong K, *et al.* Capacitive behavior of MoS_2 decorated with FeS_2@carbon nanospheres. Chem Eng J, 2020, 379: 122240
43 You B, Wang L, Yao L, *et al.* Three dimensional N-doped graphene–CNT networks for supercapacitor. Chem Commun, 2013, 49: 5016–5018
44 Liu Y, Lu Q, Huang Z, *et al.* Electrodeposition of Ni-Co-S nanosheet arrays on N-doped porous carbon nanofibers for flexible asymmetric supercapacitors. J Alloys Compd, 2018, 762: 301–311
45 Xiong G, He P, Liu L, *et al.* Plasma-grown graphene petals templating Ni–Co–Mn hydroxide nanoneedles for high-rate and long-cycle-life pseudocapacitive electrodes. J Mater Chem A, 2015, 3: 22940–22948
46 Hua M, Cui F, Huang Y, *et al.* Crafting nanosheet-built $MnCo_2S_4$ disks on robust N-doped carbon matrix for hybrid supercapacitors. Electrochim Acta, 2019, 323: 134770
47 Chandra Sekhar S, Nagaraju G, Ramulu B, *et al.* Multifunctional core-shell-like nanoarchitectures for hybrid supercapacitors with high capacity and long-term cycling durability. Nano Res, 2019, 12: 2597–2608
48 Liu S, Jun SC. Hierarchical manganese cobalt sulfide core–shell nanostructures for high-performance asymmetric supercapacitors. J Power Sources, 2017, 342: 629–637
49 Gao F, Xu B, Wang Q, *et al.* Potentiostatic deposition of $CoNi_2S_4$ nanosheet arrays on nickel foam: effect of depostion time on the morphology and pseudocapacitive performance. J Mater Sci, 2016, 51: 10641–10651
50 Gao Z, Chen C, Chang J, *et al.* Enhanced cycleability of faradic $CoNi_2S_4$ electrode by reduced graphene oxide coating for efficient asymmetric supercapacitor. Electrochim Acta, 2018, 281: 394–404
51 Jing C, Guo X, Xia L, *et al.* Morphologically confined hybridization of tiny $CoNi_2S_4$ nanosheets into S, P co-doped graphene leading to enhanced pseudocapacitance and rate capability. Chem Eng J, 2020, 379: 122305

Acknowledgements This work was supported by the National Natural Science Foundation of China (61376068, 11304132, 11304133 and 11504147), and the Fundamental Research Funds for the Central Universities (lzujbky-2017-178 and lzujbky-2017-181).

Author contributions Wang X and Tian L participated in the design of this study, and they both conducted the experiments, performed data analysis and drafted the manuscript. Long X participated in part of the experiments and collected important background information. Yang M, Song X and Xie W participated in literature search, data acquisition and analysis, and manuscript preparation. Liu D and Fu Y provided assistance for data acquisition and data analysis. Li J proposed the idea, supervised the research and revised the manuscript. Li Y supervised the research and revised the manuscript. He D performed manuscript review. All authors have read and approved the content of the manuscript.

Conflict of interest The authors declare no conflict of interest.

Supplementary information Experimental details and supporting data are available in the online version of the paper.

Xiao Wang is currently a master student at the School of Physical Science & Technology, Lanzhou University. Her research interest focuses on the development of novel metallic sulfide nanomaterials and the related high-performance aqueous supercapacitors.

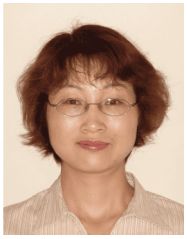

Yali Li received her bachelor and master degrees of science both from Lanzhou University and doctor degree of engineering from Saitama University, Japan. From 2009.01 to 2012.03, she worked at Nanyang Technological University, Singapore as a research fellow. Now, she holds a faculty position at the School of Physical Science & Technology, Lanzhou University. Her current research focuses on energy-harvesting and storage devices.

Junshuai Li is currently a professor at the School of Physical Science & Technology, Lanzhou University. Prior to holding this position, he performed the research on preparation of high-quality PV materials and structures, design and fabrication of advanced Si nanostructure-based PV devices at Saitama University, Japan (2006.10–2008.09) and Nanyang Technological University, Singapore (2008.09–2012.03). Now his main research interest focuses on the optical and electrical behaviors in subwavelength semiconductor structures, and renewable energy devices.

碳布上生长的开裂树皮状三元金属硫化物($NiCoMnS_4$)纳米结构用于高性能水系非对称超级电容器

王啸[†], 田凌[†], 龙霄, 杨明哲, 宋小强, 谢文璐, 刘德全, 付玉军, 栗军帅[*], 李亚丽[*], 贺德衍

摘要 本论文报道了一种高性能的自支撑超级电容器电极. 通过一步水热工艺和随后的简单电化学处理, 在碳布上制备了具有开裂树皮形状的镍-钴-锰三元金属硫化物($NiCoMnS_4$)纳米结构. 该电极在1 A g^{-1}电流密度下, 可实现高达2470.4 F g^{-1}的比容量, 并展现出良好的倍率性能和循环稳定性. 组装的基于活性炭//$NiCoMnS_4$构型的水系非对称超级电容器的电压窗口可达1.7 V; 在850.1 W kg^{-1}功率密度下, 获得了68.2 W h kg^{-1}的能量密度; 在4 A g^{-1}电流密度下, 经过10,000次循环后, 容量保持率达92.5%. 该电极材料制备方法简单且具有良好的储能性能, 因此本研究对开发电化学性能良好的自支撑金属硫化物电极及相关高性能水系超级电容器具有重要的参考价值.

